

Multiscale Energy and Eigenspace Approach to Detection and Localization of Myocardial Infarction

L. N. Sharma*, R. K. Tripathy, and S. Dandapat, *Member, IEEE*

Abstract—In this paper, a novel technique on a multiscale energy and eigenspace (MEES) approach is proposed for the detection and localization of myocardial infarction (MI) from multilead electrocardiogram (ECG). Wavelet decomposition of multilead ECG signals grossly segments the clinical components at different subbands. In MI, pathological characteristics such as hyperacute T-wave, inversion of T-wave, changes in ST elevation, or pathological Q-wave are seen in ECG signals. This pathological information alters the covariance structures of multiscale multivariate matrices at different scales and the corresponding eigenvalues. The clinically relevant components can be captured by eigenvalues. In this study, multiscale wavelet energies and eigenvalues of multiscale covariance matrices are used as diagnostic features. Support vector machines (SVMs) with both linear and radial basis function (RBF) kernel and K-nearest neighbor are used as classifiers. Datasets, which include healthy control, and various types of MI, such as anterior, anterolateral, anterioseptal, inferior, inferolateral, and inferoposterio-lateral, from the PTB diagnostic ECG database are used for evaluation. The results show that the proposed technique can successfully detect the MI pathologies. The MEES approach also helps localize different types of MIs. For MI detection, the accuracy, the sensitivity, and the specificity values are 96%, 93%, and 99% respectively. The localization accuracy is 99.58%, using a multiclass SVM classifier with RBF kernel.

Index Terms—Covariance, electrocardiogram (ECG), K-nearest neighbor (KNN), multilead ECG, multiscale eigenvalues, multiscale wavelet energy, myocardial infarction (MI), radial basis function (RBF), support vector machine (SVM).

I. INTRODUCTION

MYOCARDIAL infarction (MI), commonly known as heart attack, is due to the occlusion of one of the coronary arteries or one of its smaller branches [1], [2]. The pathogenesis for most of the MI cases is due to the progressive atherosclerotic plaques in coronary arteries. The myocardium loses perfusion and it is deprived of oxygen and other nutrients. This may also cause a local blood clot known as thrombus due to deposition of fibrin, blood platelets, and red blood cells [1]. Sometimes, thrombolytic substance is detached from the artery and flows to a distal coronary arterial tree. The consequences are the blocks in arteries at some other points, which is called coronary embolus. This interrupts the blood flow and results in myocardial

necrosis. Blood samples show elevated cardiac enzymes (biochemical marker of MI) like creatine kinase-MB and cardiac troponin T [3]–[5]. The elevated levels of above enzymes in blood serum are noticed only after 6 to 9 h. This time delay can be avoided by detecting onset of MI directly from the electrocardiogram (ECG). For detection at on-set stage, the ECG of the patients with suspected MI should be interpreted within 10 min [6].

In a standardized system of 12-lead ECG, each lead views the heart at a unique angle. This helps localize the pathological condition. During MI, multilead recordings of heart potentials will deviate from their standard characteristics. The location of infarction depends on the coronary artery (Fig. 1, marked with circle and “D” as an example) that has been occluded. This evidence can appear in different ECG leads. This requires simultaneous investigation of all the 12 leads.

Various methods are proposed for the detection of MI. These include the time-domain method [7], [8], [9], the ST-segment analysis [10] [11], the wavelet-transform-based method [12], [13], and the neural network approach [14]–[16]. Some of them are based on modeling techniques by training and testing the system. These algorithms use a few ECG leads. Instead of entire ECG segment, the analysis is based on ECG components such as ST-segment, ST-T complex, etc. This demands for an accurate detection of ST segments. This requires prior information about the presence of MI in the selected leads. Since various categories of MI evolved in different leads, it is expected that monitoring all 12 leads over time will yield a better result in the detection and localization [6]. In this study, a multiscale energy and eigenspace (MEES) [17], [18] approach for 12-lead ECG is proposed for the detection and localization of MI. The work carried out does not consider the real-time cases with patients suffering from MI. Permission from the medical board is required for real-time implementation on human subjects. The results are presented using a standard database to demonstrate the ability of the proposed method to classify the MI pathology. The rest of this paper is organized as follows. The proposed method is described in Section II, and results are produced in Section III. A brief conclusion is made in Section IV.

II. METHOD

MI is the genesis of coronary artery disease. In Fig. 1, coronary arteries and their anatomic relations with ECG leads are shown. The left main coronary artery splits into left anterior descending and left circumflex coronary arteries (see Fig. 1). The anterior left ventricle (LV), the lateral and posterior LV walls, the interventricular septum, and the apex get blood supply from these two arteries. The right coronary artery (RCA) supplies

Manuscript received May 26, 2014; revised January 20, 2015; accepted February 14, 2015. Date of publication February 24, 2015; date of current version June 16, 2015. Asterisk indicates corresponding author.

*L. N. Sharma is with the Department of Electronics and Electrical Engineering, Indian Institute of Technology Guwahati, Guwahati 781039, India (e-mail: lns@iitg.ernet.in).

R. K. Tripathy and S. Dandapat are with the Department of Electronics and Electrical Engineering, Indian Institute of Technology Guwahati.

Color versions of one or more of the figures in this paper are available online at <http://ieeexplore.ieee.org>.

Digital Object Identifier 10.1109/TBME.2015.2405134

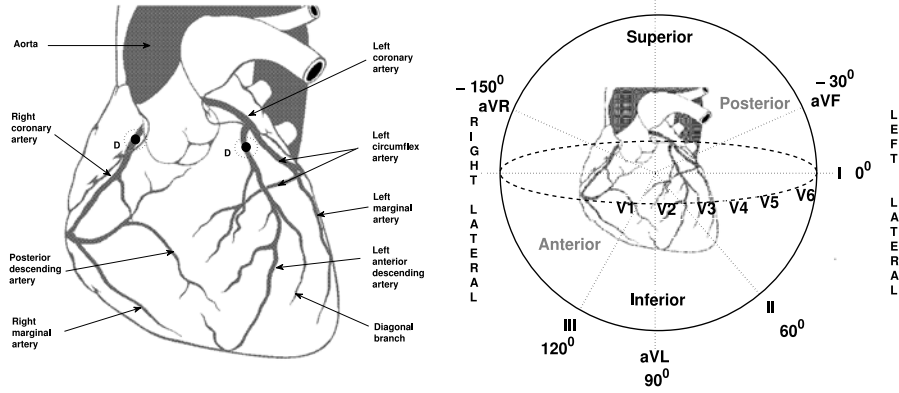


Fig. 1. Coronary arteries of human heart and 12-standard ECG leads in different planes. The probable infarction is marked with circle and **D** as an example.

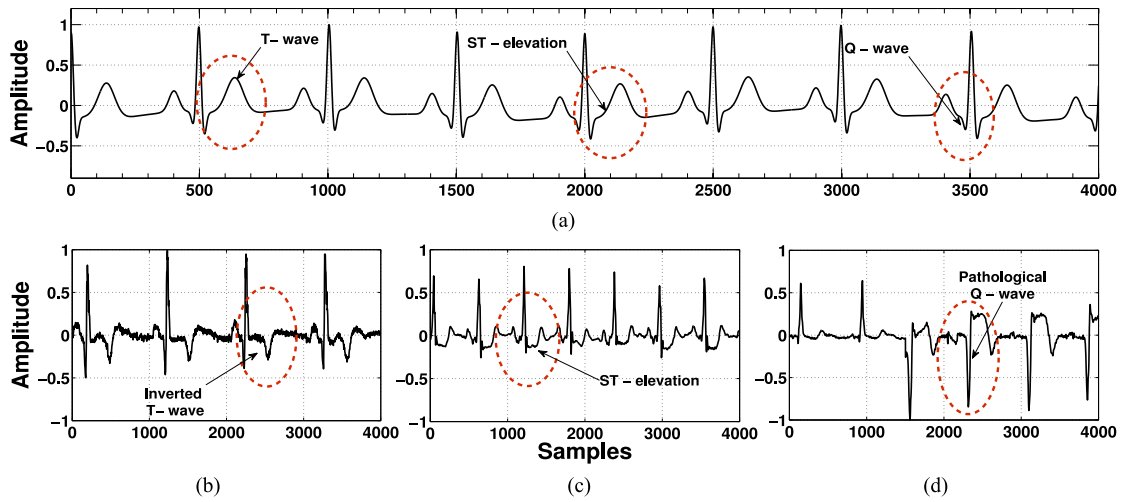


Fig. 2. Normal synthetic ECG with three stages of MI evolution. (a) Normal synthetic ECG signal for reference. (b) MI with T-wave peaking and inversion. (c) MI with change in ST elevation. (d) MI with pathological Q-wave formation.

blood and nutrients to right ventricle, inferior wall of LV, part of the posterior wall of the LV through the posterior descending artery and posterior interventricular septum [1]. The myocardial injury can occur in any of the above arteries. Various types of MIs are anterior MI, inferior MI, posterior MI, and left lateral MI. The ECG leads V1, V2, V3, and V4 show the signatures of anterior MI and the inferior MI is diagnosed from ECG leads II, III, and aVF. The pathological characteristics of left lateral MI are observed from ECG leads I, aVL, V5, and V6. Posterior MI is due to necrosis in RCA. No ECG lead captures the information of the posterior wall. Hence, it is diagnosed by evaluating the reciprocal changes in the anterior lead V1. Based on ST elevation, MIs are categorized as ST-elevated MI (STEMI) and non-STEMI [5]. The STEMI [19] evolves through the sequence:

- 1) T-wave peaking (hyperacute T-wave) followed by T-wave inversion [see Fig. 2(b)];
- 2) ST-segment elevation [see Fig. 2(c)];
- 3) appearance of pathological Q-waves [see Fig. 2(d)].

Fig. 2 shows a normal synthetic ECG signal along with three stages of pathological evolution of MI. The synthetic ECG [see Fig. 2(a)] is shown only for reference for wave morphologies.

During an infarction, any one of above changes [see Fig. 2(b)–(d)] may be present in a clinical setting. This shows the significance of evaluation of 12-lead ECG for the detection and localization of MI.

The section below presents the proposed method for the detection and localization of MI from multilead ECG. In Fig. 3, block diagrams for detection and localization are shown. The detection block [see Fig. 3(a)] comprises of preprocessing, multiscale feature analysis, and classification. The preprocessing involves filtering and frame-based segmentation. In the filtering part, the artifacts such as base line wandering and drift are filtered out by a moving average filter [20]. To remove high-frequency noise, relative energies of wavelet subbands and a noise variance-based threshold are used [21]. The frame-based processing of 12-lead ECG can capture the intrarhythm, intersample, and interlead correlation information. This information can be used to diagnose various cardiac diseases [11], [22]. In a frame-based system, data acquisition hardware gathers large number of samples at a higher rate. The detected MI-based multilead ECG frames will be input to the localization framework. The localization block [see Fig. 3(b)] consists of beat segmentation,

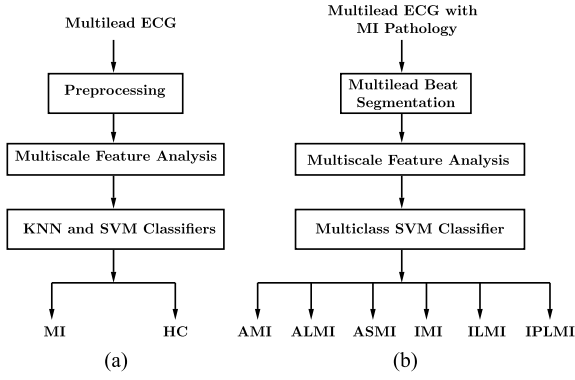


Fig. 3. Detection and localization of MI from multilead ECG. (a) Detection. (b) Localization.

multiscale feature analysis, and classification using a multiclass SVM classifier.

A. Proposed Multiscale Feature Analysis

The multiscale feature analysis involves wavelet transform of multilead ECG, evaluation of multiscale energy features, and multiscale eigendecomposition.

1) **Wavelet Transform of Multilead ECG:** Wavelet analysis of an ECG signal with J -level decomposition using suitable mother wavelet gives k th wavelet coefficient at j th level [12]. The dyadic wavelet transform using a multiresolution pyramidal decomposition technique based on a filter bank implementation gives $J + 1$ subbands. For m th ECG lead, it results with an approximation subband coefficients, $cA_{J,k}^m$, at level J and with details subbands, $cD_{j,k}^m$, at level j , where $j = 1, 2, \dots, J$. The approximation and the detail wavelet coefficients are obtained by the inner product of an input ECG signal with scaling function $\phi_{J,k}(n) = 2^{-\frac{J}{2}} \phi(2^{-J}n - k)$ and wavelet functions $\psi_{j,k}(n) = 2^{-\frac{j}{2}} \psi(2^{-j}n - k)$. The approximation and detail wavelet coefficients for the input signal $\mathbf{x}^m(n)$ are evaluated as $cA_{J,k}^m = \langle \mathbf{x}^m(n), \phi_{J,k}(n) \rangle$ and $cD_{j,k}^m = \langle \mathbf{x}^m(n), \psi_{j,k}(n) \rangle$ [12], [23]. In this study, a six-level wavelet decomposition is used. The diagnostic information of an ECG signal is distributed in different wavelet subbands based on their bandwidth or frequency content. It has been reported that the lower frequency subbands contain most of the diagnostically significant information of the ECG signal [21], [23]. If all 12-standard ECG leads are decomposed with same mother wavelet and decomposition levels, it results in similar subbands with an equal number of coefficients. It helps the formation of multiscale multivariate matrices [18]. Wavelet coefficients obtained from all ECG leads with J -level wavelet decomposition are arranged in $J + 1$ subband matrices. The columns in a subband matrix correspond to ECG leads and the rows represent the subband coefficients. The approximation subband matrix is given by $\mathbf{A}_J = [cA_{J,k}^1, cA_{J,k}^2, \dots, cA_{J,k}^m]$ and the details subband matrices are $\mathbf{D}_j = [cD_{j,k}^1, cD_{j,k}^2, \dots, cD_{j,k}^m]$, where $m = 12$ is the number of leads.

2) **Multiscale Energy:** The multiscale matrices contain grossly segmented diagnostic components of the multilead ECG.

The energy due to the wavelet coefficients along each lead for approximation and detail subbands is considered as multiscale energy, and it is given as [12]

$$E_{cA_{J,k}}^m = \frac{\sum_{k=1}^{N_J} [cA_{J,k}^m]^2}{N_J} \quad (1)$$

$$E_{cD_{j,k}}^m = \frac{\sum_{k=1}^{N_j} [cD_{j,k}^m]^2}{N_j} \quad (2)$$

where N_J and N_j are the number of coefficients in approximation and detail subbands. In this study, the multiscale energy features from $cA_{6,k}$, $cD_{6,k}$, $cD_{5,k}$, and $cD_{4,k}$ subbands are evaluated. It is seen that the "PQRST" morphologies and its changes can be captured by multiscale wavelet energies [21], [23]. The within-class variations of normalized multiscale wavelet energy for all ECG leads are evaluated using 1074 MI and 1074 healthy control (HC) multilead ECG frames. These signals are taken from the PTB (Physikalisch-Technische Bundesanstalt) diagnostic ECG database [24]. The results of MI and HC are shown in Fig. 4(a)–(d) and (e)–(h), respectively. It is observed that mean values and variances are different for different classes. For cA_6 scale, mean and variance values for lead-I signal are 0.2 and 0.044, respectively, for MI. For HC, mean and variance values are 0.115 and 0.008, respectively. For lead-I of cD_6 scale, the mean and variance values are 0.235 and 0.043, respectively, for MI, while for HC, mean and variance values are 0.117 and 0.010, respectively. Differences in mean and variance values are observed between MI and HC in all the subbands and in all the leads. In lead I and aVF along cA_6 scale, the differences in mean values between HC and MI are 0.085 and 0.140, respectively. This may be due to the difference in pathological frames between lead I and aVF. These differences between the leads show that MI pathologies can be localized. The above analysis reveals that these multiscale energy features can help detect and localize MI pathologies.

3) **Multiscale Eigenspace Analysis:** If subband matrices \mathbf{A}_J and \mathbf{D}_j are subjected to multiscale eigenanalysis, the segmented diagnostic information is expected to appear more precisely in eigenspaces. The covariance matrices from mean removed data are evaluated as [18]

$$\mathbf{C}_{A_J} = \frac{1}{(N_J - 1)} \left([\mathbf{A}_J] [\mathbf{A}_J]^T \right) \quad (3)$$

$$\mathbf{C}_{D_j} = \frac{1}{(N_j - 1)} \left([\mathbf{D}_j] [\mathbf{D}_j]^T \right) \quad (4)$$

where \mathbf{C}_{A_J} is the covariance matrix at J th approximation level and \mathbf{C}_{D_j} is the covariance matrix at j th details scale [17], [18]. The eigendecomposition of covariance matrices are

$$\mathbf{C}_{A_J} \mathbf{V}_{A_J} = \mathbf{V}_{A_J} \mathbf{\Lambda}_{A_J} \quad (5)$$

$$\mathbf{C}_{D_j} \mathbf{V}_{D_j} = \mathbf{V}_{D_j} \mathbf{\Lambda}_{D_j} \quad (6)$$

where \mathbf{V}_{A_J} , \mathbf{V}_{D_j} and $\mathbf{\Lambda}_{A_J}$, $\mathbf{\Lambda}_{D_j}$ are the eigenvectors and eigenvalues for matrices of approximation and details subband matrices, respectively. The orthonormal eigenvectors represent the signals in the directions of maximum variances. Most of the energies are retained in wavelet subbands $cA_{6,k}^m$, $cD_{6,k}^m$, $cD_{5,k}^m$,

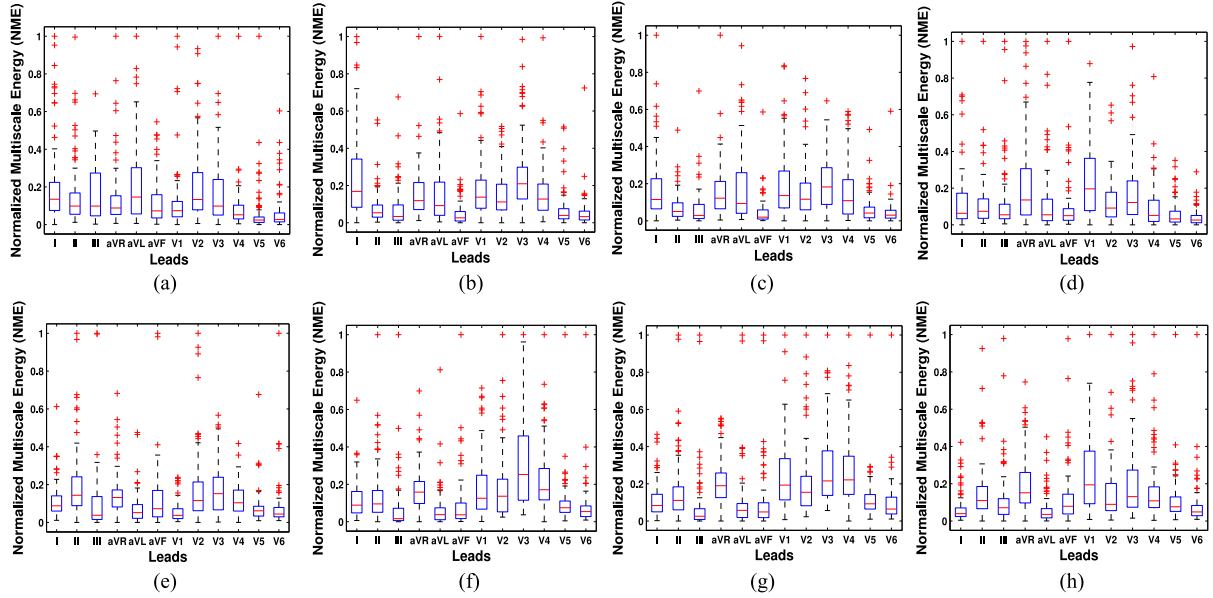


Fig. 4. Normalized multiscale energy for large data set which shows within-class variation. (a)–(d) Variation of multiscale energy for $cA_{6,k}$, $cD_{6,k}$, $cD_{5,k}$, and $cD_{4,k}$ subbands for all ECG leads for MI cases. (e)–(h) Variation of multiscale energy for $cA_{6,k}$, $cD_{6,k}$, $cD_{5,k}$, and $cD_{4,k}$ subbands for all ECG leads for HC cases.

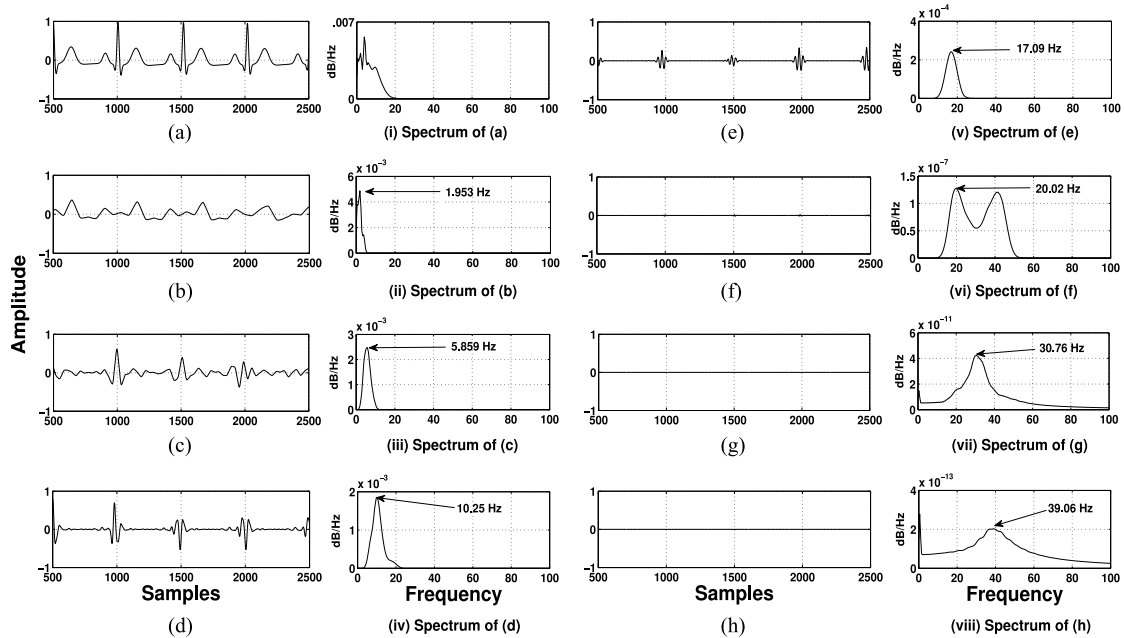


Fig. 5. Synthetic reconstructed ECG signals with corresponding spectrums at scales when ECG data are subjected to multiscale eigenanalysis. (a) Synthetic ECG with its spectrum in panel (i). (b) Reconstructed ECG considering eigenvalues only at scale A_6 with its spectrum in panel (ii). (c) Reconstructed ECG considering eigenvalues only at scale D_6 with its spectrum in panel (iii). (d) Reconstructed ECG considering eigenvalues only at scale D_5 with its spectrum in panel (iv). (e) Reconstructed ECG considering eigenvalues only at scale D_4 with its spectrum in panel (v). (f) Reconstructed ECG considering eigenvalues only at scale D_3 with its spectrum in panel (vi). (g) Reconstructed ECG considering eigenvalues only at scale D_2 with its spectrum in panel (vii). (h) Reconstructed ECG considering eigenvalues only at scale D_1 with its spectrum in panel (viii).

and $cD_{4,k}^m$, where m is the ECG lead number [21], [23]. From each of the multiscale matrices A_6 , D_6 , D_5 , and D_4 , six dominant eigenvalues are used as features. Fig. 5 shows a normal synthetic ECG signal and the reconstructed signals at different scales with the corresponding spectra. The synthetic ECG signal is generated based on the dynamic model given in the literature [25]. It is generated with sampling frequency 500 Hz and mean

heart rate at 60 beats/min. All other parameters are kept default as in a reference program. Using the cut-and-align method, a multivariate matrix is formed from the synthetic ECG signal. A six-level wavelet decomposition is performed using Daubechies 9/7 biorthogonal wavelet filters and subbands are arranged in multiscale multivariate matrices. The signals are reconstructed with the eigenvalues only from the same subband matrix. The

reconstructed signal and its spectrum of A_6 -scale are shown in Fig. 5(b) and (ii), respectively. The reconstructed signals show grossly segmented P-wave and T-wave [see Fig. 5(b)]. The center frequency for the spectrum is found at 1.953 Hz [see Fig. 5(ii)]. The low-frequency part of QRS complexes and the higher frequency part of P-wave and T-wave are seen in D_6 -scale [see Fig. 5(c) and (iii)]. The center frequency is 5.859 Hz. The D_5 -scale contains QRS complex and its center frequency is 10.25 Hz [see Fig. 5(c) and (iv)]. The higher frequency part of QRS complex is found in D_4 -scale [see Fig. 5(e)] and the center frequency is 17.09 Hz [see Fig. 5(v)]. All other scales D_3 – D_1 show predominantly the noise part of the signals. These results show the gross segmentation of clinical information across the matrices. The subband matrices contain these clinical information. The eigenvalues of the subband matrices can be related to the clinical information present in the matrices. It is expected that any variation in diagnostically important components, P-wave, T-wave, QRS-complex, and ST-segment, will be reflected in eigenvalues. In case of pathology, the low-frequency components T-wave, ST-segment, and Q-wave appear in low-frequency subband matrices like A_6 , D_6 , D_5 , and D_4 . In this study, the first six eigenvalues from each of covariance matrix are used to form feature vectors since most of the energy is retained by them.

The changes in covariance structures due to various ECG morphologies result in different eigenvalues. Fig. 6(a) and (b) shows “LEV versus principal components” for A_6 , D_6 , D_5 , and D_4 subband matrices, for HC and MI cases. LEV is the log of eigenvalues. Comparison of results in these two figures shows that the eigenvalues for MI cases are different from HC cases. Hence, these eigenvalues can be used as representative features for clinical information in the signals. Over a large dataset, changes in eigenvalues are shown in Fig. 7. The within-class variations of eigenvalues for HC cases at each scale are shown by the box plot in Fig. 7(a)–(d). Similarly, the within-class variations of eigenvalues for MI cases at each scale are shown by the box plot in Fig. 7(e)–(h). For pathological cases, the mean and variance values of first six principal components (PCs) at A_6 , D_6 , D_5 , and D_4 , differ from the HC cases. For A_6 scale, mean and variance values of first PC for MI are 7.3377 and 1.1574, respectively, whereas mean and variance values for HC are 7.8024 and 1.0712. The difference between mean values for D_5 scale in PC1, PC2, and PC3 are 0.65, 0.3, and 0.26, respectively, between HC and MI. Similar differences are also observed in other scales. These variations are due to the difference in covariance structures. The covariance structures depend on the subband diagnostic information and interlead correlations. The interlead correlations will depend on characteristics of the signals in the leads. The above analysis shows that the multiscale eigenvalues are suitable for detection and localization MI pathology. The multiscale energies and eigenvalues capture the information related to various ECG morphologies. In this study, the feature vector z_i consists of 72-elements which include 48 multiscale wavelet energy elements and 24 eigenvalue elements. These features are selected from four diagnostically important scales or subband matrices such as A_6 , D_6 , D_5 , and D_4 . The 48 multiscale energy elements and 24 eigenvalues are chosen

from these four subband matrices with 12 energy elements and six dominant eigenvalues from each subband matrix. This constitutes a MEES feature vector. The statistical significance of the proposed MEES features is evaluated using the paired student t-test approach. A feature is said to be “statistically significant,” if it has higher t-value and lower p-value [26]. In this study, out of 48 multiscale energy features, ten features have p-value greater than 0.005 and 37 features have p-value less than 0.001. These 37 multiscale energy features with lower p-value are statistically significant for MI detection. The QRS-complex and some part of T-wave information are present in cD5 subband. It is observed that a maximum of ten out of 12 multiscale energy features in cD5 subband are significant. Similarly, out of 24 multiscale eigenspace features, 15 features have p-value less than 0.001. These 15 features are statistically significant for detection of MI. The first three eigenspace features of D_4 and D_5 scale have lower p-value. This may be due to the presence of QRS-complex information in both D_4 and D_5 scales. For choosing an optimal feature subset, the correlation-based feature selection (CFS) method is employed [27].

B. Classifiers and Performance Measures

In this study, two classifiers as K-nearest neighbor (KNN) and support vector machine (SVM) with linear and radial basis function (RBF) kernel are used for detection and classification. For localization of different types of myocardial infarction as anterior (AMI), anteriolateral (ALMI), anterioseptal (ASMI), inferior (IMI), inferiolateral (ILMI), and inferioposteriolateral (IPLMI), the multiclass SVM classifier is used. The KNN and the SVM are supervised learning models, which are used for identifying the class levels of the test feature vectors. These classifiers are used for cardiac arrhythmia detection [9], [28]. The SVM is a two-class classifier. It works with an objective to maximize the hyperplane [29] corresponding to the decision boundary. The multiclass classification using SVM is accomplished through various multiclass coding techniques like “one vs one,” “one vs all,” etc. [30]. The feature matrix for multilead ECG consists of the input, $Z \in \mathbb{R}^{p \times q}$ with each instance feature vector $z_i \in \mathbb{R}^q$, $i \in 1, 2, \dots, p$, where p is number of instances. In this study, the length of feature vector is q and ($q = 72$). A fivefold cross-validation scheme is used to select the number of instances for training and testing of classifiers. The output for each instance is $y_i \in (-1, 1)$ for MI detection. For SVM with nonlinear and nonseparable cases, each input is mapped to a transformed space with the help of kernel function [29], [31]. For training set in each fold of cross validation, the primal optimization problem for SVM corresponds to the maximized hyperplane [29], [30]. For MI and HC, it is given as

$$\text{minimize } \frac{w^T w}{2} + C \sum_{i=1}^p \varepsilon_i \quad (7)$$

subject to $y_i (w^T \tilde{\phi}(z_i) + b) \geq 1 - \varepsilon_i$, $\varepsilon_i \geq 0$ and C is a regularization parameter. The Lagrangian is used to solve the primal optimization problem. After solving the Lagrangian, the dual quadratic programming optimization problem [30], [32] can be

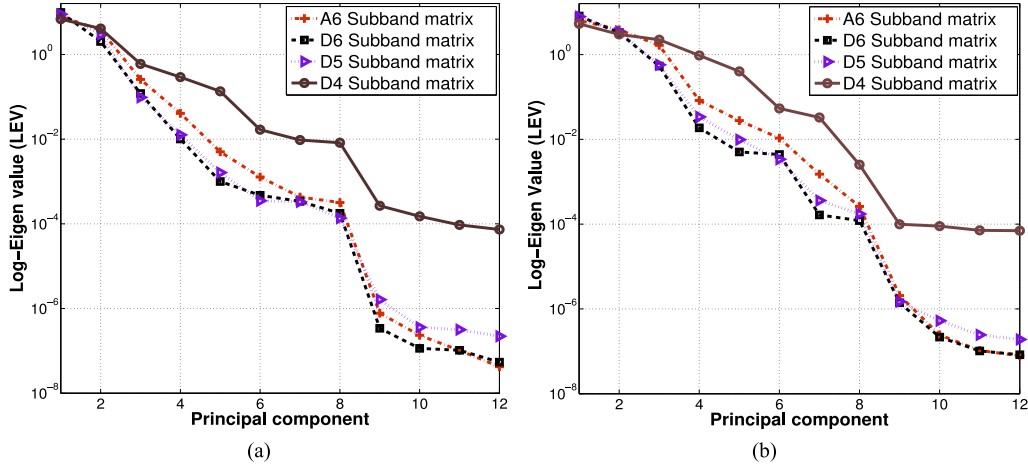


Fig. 6. Log-eigenvalue plot for HC and MI. Wavelet decompositions up to six level are performed for the PTB multilead ECG database. (a) LEV plot for healthy control. (b) LEV plot for myocardial infarction.

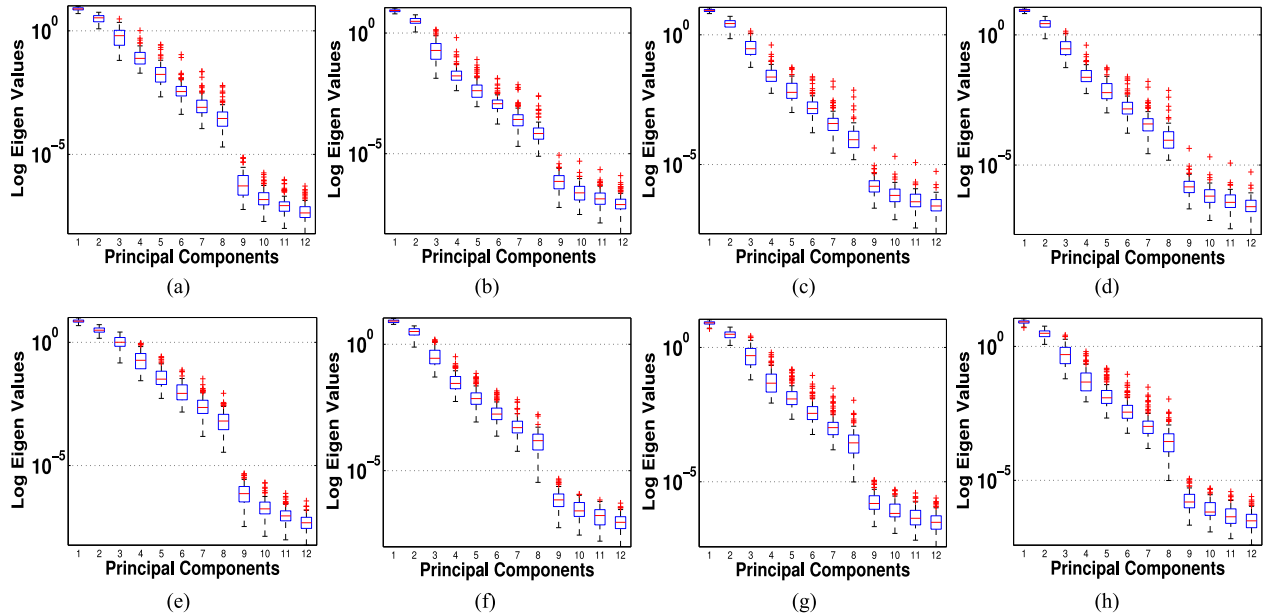


Fig. 7. (a)–(d) Box plot for variation of log-eigenvalues over 1074 HC multilead ECG frames at A₆, D₆, D₅, and D₄ scales, respectively. (e)–(h) Box plot for variation of log-eigenvalues over 1074 MI multilead ECG frames at A₆, D₆, D₅, and D₄ scales, respectively.

reformulated as

$$\max_{\mu} Q(\mu) = \sum_{i=1}^p \mu_i - \frac{1}{2} \sum_{i=1}^p \sum_{j=1}^p \mu_i \mu_j y_i y_j \mathbf{K}(\mathbf{z}_i, \mathbf{z}_j) \quad (8)$$

subjected to $0 \leq \mu_i \leq C$, $i = 1, 2, \dots, p$ and $\sum_{i=1}^p \mu_i y_i = 0$. The solution of dual optimization problem gives the values of Lagrange multiplier μ_i . This value is used for evaluation of weight $\mathbf{w} = \sum_{i=1}^p \mu_i y_i \mathbf{z}_i$ and bias $b = y_i - \mathbf{w}^T \tilde{\phi}(\mathbf{z}_i)$, respectively. The p th instance output y_p for the test feature vector \mathbf{z}_{test} from multilead ECG is evaluated as

$$y_p = \text{sgn} \left[\sum_{i=1}^{p^*} \mu_i y_i \mathbf{K}(\mathbf{z}_i, \mathbf{z}_{\text{test}}) \right] \quad (9)$$

where p^* corresponds to the number of support vectors and $\mathbf{K}(\mathbf{z}_i, \mathbf{z}_{\text{test}})$ is the kernel function. The linear and RBF kernel

functions used in this study are given as

$$\mathbf{K}(\mathbf{z}_i, \mathbf{z}_{\text{test}}) = \mathbf{z}_{\text{test}}^T \mathbf{z}_i \quad (10)$$

$$\mathbf{K}(\mathbf{z}_i, \mathbf{z}_{\text{test}}) = \exp \left(-\frac{\|\mathbf{z}_{\text{test}} - \mathbf{z}_i\|^2}{2\sigma^2} \right) \quad (11)$$

where σ corresponds to the width of Gaussian. C is used to maintain the tradeoff between bias and variance [31]. A large value of C corresponds to the model with low bias and higher variance, which can cause data overfitting. A small value of C corresponds to the model with high bias and low variance, which causes data under fitting. In this study, the parameter $C = 30$ for SVM with linear kernel and parameters $C = 30$ and $\sigma = 0.5$ for SVM with RBF kernel are found suitable for the minimum training error. There is no large fluctuation on testing instances for MI detection and localization for these values.

For the training of KNN classifier, the number of nearest neighbor $K = 5$ and Euclidean distance metric are used.

The performances of the classifiers are evaluated in terms of sensitivity, specificity, and accuracy. These parameters are estimated by comparing the actual test output and the predicted output. A confusion matrix visualizes the number of true positives (TPs), false positives (FPs), false negatives (FNs), and true negatives (TNs) for a classifier. The sensitivity [33] relates to the ability of trained model to identify positive results of MI. The sensitivity (SE) is evaluated as [33]

$$SE = \frac{TP}{TP + FN}. \quad (12)$$

The specificity (SP) [33] is related to the ability of identifying the negative outcomes (HC or non-infarcted). The specificity (SP) is evaluated as [33]

$$SP = \frac{TN}{TN + FP}. \quad (13)$$

The classification accuracy (Acc) of a measurement system is the degree of closeness of measurements of a quantity to that of its actual (true) value, and it is defined as

$$Acc = \frac{TP + TN}{TP + TN + FP + FN}. \quad (14)$$

The plot between SE and (1-SP) is termed as the receiver operating characteristic (ROC) curve [34]. The area under the ROC curve is widely used as a metric to measure the performance of binary classifiers [35]. In this study, the area under the ROC curves for KNN, SVM with linear kernel, and SVM with RBF kernel classifiers are evaluated.

III. RESULTS AND DISCUSSION

In this study, the standard 12-lead ECG signals are taken from the PTB diagnostic ECG database [24]. It is a collection of digitized ECG records from healthy volunteers and patients having different heart diseases at the Department of Cardiology, University Clinic Benjamin Franklin, Berlin, Germany. From 290 subjects, a total number of 549 records are compiled. Individual record has 12 conventional leads (I, II, III, aVR, aVL, aVF, V1, V2, V3, V4, V5, V6) and three Frank leads (VX, VY, VZ). The sampling rate is 1000 Hz with 16-bit resolution over a range of 16.384 mV. The subjects in different pathologies are—MI: 148; cardiomyopathy/heart failure: 18; bundle branch block: 15; dysrhythmia: 14; myocardial hypertrophy: 7; valvular heart disease: 6; myocarditis: 4; miscellaneous: 4; and HCs: 52.

A. MI Detection

In this section, MI detection is evaluated using the proposed method shown in Fig. 3(a). For R-peak detection, Tompkins's algorithm is applied [36]. For MI detection, a frame of four ECG beats from each ECG lead is considered. This covers most of the characteristics of ECG cycle. A multilead data matrix is formed with ECG samples as rows and 12 ECG leads as columns. Wavelet decomposition is carried out using Daubechies 9/7 biorthogonal wavelet filters up to six levels. Datasets related to HCs (HC) and MI pathologies are evaluated for detection.

TABLE I
PERFORMANCE EVALUATION AND CONFUSION MATRIX FOR SVM
AND KNN CLASSIFIERS

Classifiers	TP	FN	TN	FP	Sensitivity(%)	Accuracy(%)	Specificity(%)
KNN	85	15	77	23	85	81	77
SVM Lin	87	13	91	9	90.42	89	87.69
SVM RBF	93	7	99	1	93	96	99

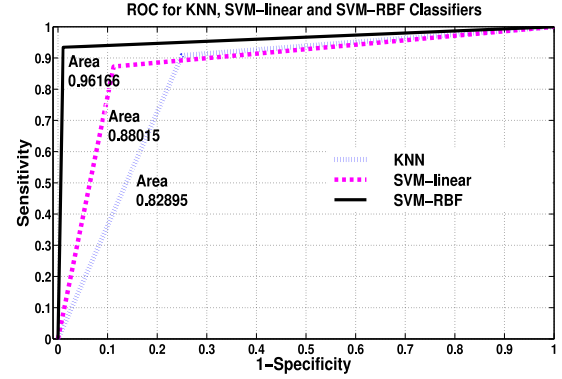


Fig. 8. ROC for KNN, SVM with linear kernel, and SVM with RBF kernel classifiers.

The 72-D MEES feature vector is extracted from each of the multilead data matrix. Each feature vector corresponds to an instance. This feature vector is used as input for the KNN and the SVM classifiers. In this study, 200 instances, each from HC and MI classes, are used for evaluation. To train the classifiers, 100 instances, each from HC and MI pathology, are used. The other 100 instances are used for testing. Table I shows the number of TP, TN, FP, and FN values for both KNN and SVM classifiers. It is observed that the SVM classifier with RBF kernel has an accuracy of 96%, sensitivity of 93%, and specificity of 99%. The SVM with the linear kernel function and the KNN classifiers have accuracy values of 89% and 81%, sensitivity values of 90.42% and 85%, and specificity values of 87.69% and 77%, respectively.

Fig. 8 shows the ROC curves for KNN, SVM with linear kernel, and SVM with RBF kernel classifier. It is noticed that the area under the ROC curves for KNN, SVM with linear kernel, and SVM with RBF kernel are 0.82895, 0.88015, and 0.96166, respectively. To perform cross validation, 2148 instances, each from MI and HC, are considered. In this study, the fivefold cross-validation scheme is used for choosing training and testing instances of classifiers. Results are shown with multiscale energy features, multiscale eigenspace features, MEES features, and with the feature subset derived using CFS. Table II shows the performance of KNN and SVM classifiers along each fold. When multiscale energy features are used, the SVM classifier with RBF kernel produces an average accuracy of 90.14%, average sensitivity of 88.68%, and average specificity of 91.62%, respectively. Similarly, when multiscale eigenspace features are used, the SVM classifier with RBF kernel shows average accuracy of 84.76%, average sensitivity of 83.68%, and average specificity of 85.85%, respectively. When all the

TABLE II
PERFORMANCE OF KNN AND SVM CLASSIFIERS OVER EACH FOLD FOR MI DETECTION

Feature Selection	Classifiers	Parameters	Fold1	Fold2	Fold3	Fold4	Fold5	Average
Energy	KNN	Accuracy(%)	85.37	84.06	83.98	84.61	83.85	84.37
		Sensitivity(%)	86.08	83.77	85.05	84.58	85.14	84.92
		Specificity(%)	84.67	84.37	82.99	84.67	82.66	83.87
Energy	SVM-Lin	Accuracy(%)	86.62	83.00	87.75	86.62	86.12	86.02
		Sensitivity(%)	86.30	83.53	88.28	85.36	85.51	85.79
		Specificity(%)	86.97	82.47	87.22	87.90	86.79	86.27
Energy	SVM-RBF	Accuracy(%)	90.50	89.79	90.40	89.84	90.21	90.14
		Sensitivity(%)	89.91	89.8	88.66	87.97	87.09	88.68
		Specificity(%)	91.11	89.78	92.14	91.74	93.35	91.62
Eigenspace	KNN	Accuracy(%)	83.45	85.05	84.52	85.95	85.73	84.94
		Sensitivity(%)	85.11	86.87	85.68	88.33	87.64	86.72
		Specificity(%)	81.94	83.38	83.42	83.81	83.84	83.27
Eigenspace	SVM-Lin	Accuracy(%)	74.62	76.75	76.62	72.12	74.87	74.99
		Sensitivity(%)	72.11	77.19	77.50	72.56	74.67	74.80
		Specificity(%)	77.39	76.34	76.12	71.93	75.14	75.38
Eigenspace	SVM-RBF	Accuracy(%)	85.73	84.47	84.06	85.66	83.92	84.76
		Sensitivity(%)	84.07	81.87	83.93	84.53	84.01	83.68
		Specificity(%)	87.4	87.06	84.19	86.79	83.84	85.85
All features	KNN	Accuracy(%)	83.37	82.15	82.62	81.25	81.75	82.28
		Sensitivity(%)	80.79	84.51	80.43	82.25	81.92	81.98
		Specificity(%)	86.13	80.37	82.50	80.36	82.25	82.32
All Features	SVM-Lin	Accuracy(%)	87.50	90.62	86.25	87.86	87.87	88.02
		Sensitivity(%)	85.08	89.93	86.32	86.08	88.75	87.23
		Specificity(%)	89.94	91.37	86.19	89.02	86.15	88.53
All Features	SVM-RBF	Accuracy(%)	96.03	96.68	96.42	95.14	96.50	96.15
		Sensitivity(%)	95.15	95.00	95.23	95.35	96.74	95.49
		Specificity(%)	96.92	98.37	97.62	94.94	96.26	96.82
CFS	KNN	Accuracy(%)	85.06	85.24	85.72	85.60	85.57	85.23
		Sensitivity(%)	84.61	85.06	85.39	85.27	84.74	85.01
		Specificity(%)	86.63	84.49	87.12	85.95	84.65	85.76
CFS	SVM-Lin	Accuracy(%)	88.62	89.04	90.16	89.25	91.23	89.66
		Sensitivity(%)	88.31	88.43	90.59	90.83	90.29	89.69
		Specificity(%)	89.05	89.59	89.43	87.68	89.72	89.49
CFS	SVM-RBF	Accuracy(%)	97.80	96.85	96.09	96.30	97.12	96.83
		Sensitivity(%)	97.23	97.57	96.12	97.21	98.03	97.23
		Specificity(%)	96.67	96.56	97.16	95.41	96.21	96.40

features are used, the SVM classifier with RBF kernel shows an average accuracy of 96.15%, average sensitivity of 95.49%, and average specificity of 96.82%. The SVM with linear kernel function and the KNN classifiers have average accuracy values of 88.02% and 82.28%, average sensitivity values of 87.23% and 81.98%, and average specificity values of 88.53% and 82.32%, respectively, for all the features. When the CFS method is employed, the average accuracy, average sensitivity, and average specificity values are of 96.83%, 97.23%, and 96.40%, respectively, for the SVM classifier with RBF kernel. It is observed that the accuracy, the sensitivity, and the specificity values of classifiers are improved with the CFS method. This may be due to the elimination of the correlated features from the 72-D feature vector. In this study, the features that are highly correlated with each other with correlation ratio of 0.9 are eliminated. After the removal of such redundant features, the 72-D feature vector is reduced to a new feature vector containing 60 features. Then, the performance of 60-D new feature vector is evaluated using KNN and SVM classifiers. The performance of SVM with RBF kernel is better than KNN and SVM with linear kernel classifiers. The RBF kernel in SVM projects the feature vector

to higher dimensional space [31]. This may be the reason for the better performance of SVM classifier with RBF kernel for MI detection. These results show that the MEES-based feature vector works well for detection of MI pathology.

Most of the methods reported in the literature are beat-specific and they are based on neural networks and other classifiers. The proposed MEES feature-based method for MI detection is compared with the other methods, and the results are shown in Table III. Results reported in this paper are close to the results of MI detection in the literature. Some of these methods used single or fewer ECG leads, which are expected to carry MI pathologies. The performance of earlier method depends on the accuracy of detection of ST segments and ST-T complex. The proposed method does not require a prior segmentation of ST segments and ST-T complex. The knowledge of the presence of MI pathology is not necessary as it is based on 12 standard ECG leads.

B. Localization of MI

MI detection is evaluated as a two-class problem. Localization of MI is a multilabel classification task. In this section,

TABLE III
COMPARISON OF THE PROPOSED APPROACH WITH EXISTING METHODS FOR DETECTION OF MI

Metric	Reddy [14]	Lu [15]	Heden [16]	Jayachandran [12]	Sun [10]	Muhammad [9]	Proposed method
Sensitivity(%)	79	84.6	95	NA	91.43	NA	93
Specificity(%)	97	90.0	86.3	NA	77.29	NA	99
Accuracy(%)	NA	NA	NA	96%	NA	99	96
Remarks	Beat Specific	Beat Specific	Beat Specific	Beat Specific	Beat Specific	Beat Specific	Frame Specific

TABLE IV
CONFUSION MATRIX OF MULTICLASS SVM WITH LINEAR KERNEL FOR MI LOCALIZATION

Actual/ Predicted	AMI	ALMI	ASMI	IMI	ILMI	IPLMI
AMI	111	1	3	0	0	6
ALMI	2	114	4	0	1	0
ASMI	3	9	105	1	2	1
IMI	2	0	0	115	3	1
ILMI	2	0	0	1	116	2
IPLMI	3	1	6	6	0	105

TABLE V
CONFUSION MATRIX OF MULTICLASS SVM WITH RBF KERNEL FOR MI LOCALIZATION

Actual/Predicted	AMI	ALMI	ASMI	IMI	ILMI	IPLMI
AMI	121	0	0	0	0	0
ALMI	1	119	0	0	0	1
ASMI	0	0	121	0	0	0
IMI	0	0	0	121	0	0
ILMI	0	0	0	0	121	0
IPLMI	0	0	0	1	0	120

TABLE VI
CLASSIFICATION ACCURACY FOR MULTICLASS SVM CLASSIFIERS

Classifiers	Accuracy(%)
SVM with Lin Kernel	91.73
SVM with RBF Kernel	99.58

TABLE VII
PERFORMANCE OF KNN AND SVM CLASSIFIERS OVER EACH FOLDS FOR MI LOCALIZATION

Feature Selection	Classifiers	Parameters	Fold1	Fold2	Fold3	Fold4	Fold5	Average
Energy	SVM-RBF	Accuracy(%)	98.07	95.45	96.83	96.69	97.93	97.00
Eigenspace	SVM-RBF	Accuracy(%)	92.56	94.07	94.62	92.97	93.80	93.60
All Features	SVM-Lin	Accuracy(%)	90.86	92.53	92.71	89.56	91.28	91.38
All Features	SVM-RBF	Accuracy(%)	98.67	99.23	99.45	99.28	99.74	99.27
CFS	SVM-Lin	Accuracy(%)	92.17	93.24	93.79	93.84	93.58	93.32
CFS	SVM-RBF	Accuracy(%)	99.54	99.78	99.62	99.57	99.81	99.66

MI pathologies are localized using the proposed method, which is depicted in Fig. 3(b). The MI detected multilead data matrix is segmented into multilead beat matrices. In the multilead beat matrix, the rows consist of single beat ECG samples and the columns correspond to 12 ECG leads. Six classes of MI pathologies, AMI, ALMI, ASMI, IMI, ILMI, and IPLMI, are used for evaluation of the proposed MI localization method.

TABLE VIII
COMPUTATIONAL TIME FOR CLASSIFIER TO DETECTION AND LOCALIZATION OF MI PATHOLOGY

Detection		Localization	
Algorithmic step	Computational Time	Algorithmic step	Computational Time
Preprocessing, Frame Segmentation and Feature Extraction	0.43 s	Multilead Beat Segmentation and Feature Extraction	0.26 s
Training	56.67 s	Training	58.5 s
Testing	0.44 s	Testing	0.025 s

The 72-D MEES feature vectors are estimated from multilead beat matrices. These feature vectors are used as input to the multiclass SVM classifier.

During the training phase of multiclass SVM classifier, 100 instances from each class of MI are considered. A total of 726 unknown instances are evaluated in the testing phase. Tables IV and V shows the confusion matrix for both linear and RBF kernel-based multiclass SVM classifiers. It is observed that the number of TPs is more in RBF kernel multiclass SVM than that of linear kernel multiclass SVM classifiers. The accuracy for each of the multiclass classifiers are shown in Table VI. The classification accuracy of RBF kernel multiclass SVM classifier is found to be 99.58%, which is more than that of linear kernel multiclass SVM classifier. This shows that the multiclass SVM successfully localizes the MI pathology. For MI localization, the fivefold cross-validation technique is also used for choosing training and testing instances of multiclass SVM classifiers. Table VII shows the MI localization accuracy of multiclass SVM classifier with linear and RBF kernel considering all features and feature subset using CFS along each fold. The highest average accuracy of 99.66% is found using multiclass SVM with RBF kernel for feature set using CFS. For the MI localization case, the SVM classifier with RBF kernel produces an average accuracy value of 97% for the multiscale energy features. When the multiscale eigenspace features are used, the SVM classifier shows an average accuracy of 93.60%. The average accuracy value for combined MEES features is 99.27%, which is higher than the performance of individual feature sets. The higher accuracy values obtained using CFS is due to the elimination of redundant features. From this above observations, it can be concluded that the proposed MEES approach is effective to localize MI using 12 lead ECG.

The proposed algorithm is implemented in MATLAB 2010a software in Windows platform on a desktop computer having

Intel i5 processor (@3.20 GHz) and 4-GB RAM. The computational times for each stage of MI detection and localization are shown in Table VIII. The training stage of the classifier takes highest time for both detection and localization, 56.67 and 58.5 s, respectively. The lowest time, 0.025 s, is required in the testing stage of localization.

IV. CONCLUSION

In this paper, a novel approach is proposed for the detection and localization of MI from multilead ECG. Most of the present works are based on fewer ECG leads, which are expected to have MI characteristics. The proposed MI detection and localization approach from multilead ECG does not require any prior information about the pathologies in leads. This approach is based on the evaluation of multiscale energy and MEES features. Analysis with number of data shows that these features are capable of not only discriminating HC and MI, but also they can differentiate between different types MI pathologies. For MI detection, the multilead data matrix is used. The performance of MEES feature vector is evaluated using KNN and SVM classifiers with linear and RBF kernel functions. For localization, the MI-detected multilead data matrix is divided into multilead beat matrices. Various pathological MI cases such as AMI, ALMI, ASMI, IMI, ILMI, and IPLMI are used for detection and localization. The MEES features shows an accuracy of 96% for MI detection using an SVM classifier with RBF kernel. A localization accuracy of 99.58% is found. The proposed method is simpler compared to earlier method for MI detection. This method does not require prior detection of ST segment.

ACKNOWLEDGMENT

The authors are grateful to editor-in-chief and associate editor for encouragement and would like to thank anonymous reviewers for their suggestions to improve the quality of this manuscript.

REFERENCES

- [1] A. C. Guyton and J. E. Hall, *Text Book of Medical Physiology*, 11th ed. New York, NY, USA: Elsevier, 2006.
- [2] A. L. Goldberger, *Clinical Electrocardiography: A Simplified Approach*. New York, NY, USA: Elsevier Health Sciences, 2012.
- [3] E. Antman *et al.*, "Myocardial infarction redefined: a consensus document of the joint European society of cardiology/American college of cardiology committee for the redefinition of myocardial infarction: The joint European Society of Cardiology/American College of Cardiology Committee," *J. Am. Coll. Cardiol.*, vol. 36, no. 3, pp. 959–969, 2000.
- [4] S. G. Goodman *et al.*, "The diagnostic and prognostic impact of the redefinition of acute myocardial infarction: Lessons from the global registry of acute coronary events (grace)," *Am. Heart J.*, vol. 151, no. 3, pp. 654–660, 2006.
- [5] K. Thygesen *et al.*, "Third universal definition of myocardial infarction," *Circulation*, vol. 126, no. 16, pp. 2020–2035, 2012.
- [6] K. Thygesen *et al.*, "Third universal definition of myocardial infarction," *J. Am. Coll. Cardiol.*, vol. 60, no. 16, pp. 1581–1598, 2012.
- [7] P. D. Chazal *et al.*, "Automatic classification of heartbeats using ECG morphology and heartbeat interval features," *IEEE Trans. Biomed. Eng.*, vol. 51, no. 7, pp. 1196–1206, Jul. 2004.
- [8] S. Mitra *et al.*, "A rough-set-based inference engine for ECG classification," *IEEE Trans. Instrum. Meas.*, vol. 55, no. 6, pp. 2198–2206, Dec. 2006.
- [9] A. Muhammad *et al.*, "Detection and localization of myocardial infarction using k-nearest neighbor classifier," *J. Med. Syst.*, vol. 36, no. 1, pp. 279–289, 2012.
- [10] L. Sun *et al.*, "ECG analysis using multiple instance learning for myocardial infarction detection," *IEEE Trans. Biomed. Eng.*, vol. 59, no. 12, pp. 3348–3356, Dec. 2012.
- [11] F. Badilini *et al.*, "Beat-to-beat quantification and analysis of ST displacement from Holter ECGs: A new approach to ischemia detection," in *Proc. Comput. Cardiol.*, 1992, pp. 179–182.
- [12] E. S. Jayachandran *et al.*, "Analysis of myocardial infarction using discrete wavelet transform," *J. Med. Syst.*, vol. 34, no. 6, pp. 985–992, 2010.
- [13] C. Papaloukas *et al.*, "Automated methods for ischemia detection in long duration ECGs," *Cardiovascular Review Rep.*, vol. 24, no. 6, pp. 313–319, Jun. 2003.
- [14] M. R. S. Reddy *et al.*, "Neural network versus electrocardiographer and conventional computer criteria in diagnosing anterior infarct from the ECG," in *Proc. Comput. Cardiol.*, Oct. 1992, pp. 667–670.
- [15] H. L. Lu *et al.*, "An automated ECG classification system based on a neuro-fuzzy system," in *Proc. Proc. Comput. Cardiol.*, 2000, pp. 387–390.
- [16] B. Heden *et al.*, "Acute myocardial infarction detected in the 12-lead ECG by artificial neural networks," *Circulation*, vol. 96, pp. 1798–1802, 1997.
- [17] B. R. Bakshi, "Multiscale PCA with application to multivariate statistical process monitoring," *AIChE J.*, vol. 44, pp. 1596–1610, 1998.
- [18] L. N. Sharma *et al.*, "Multichannel ECG data compression based on multiscale principal component analysis," *IEEE Trans. Inf. Technol. Biomed.*, vol. 16, no. 4, pp. 730–736, Jul. 2012.
- [19] F. Morris *et al.*, *ABC of Clinical Electrocardiography* (ser. ABC Series). New York, NY, USA: Wiley, 2003.
- [20] R. M. Rangayyan, *Biomedical Signal Analysis: A Case-Study Approach* (ser. IEEE Press Series in Biomedical Engineering). Piscataway, NJ, USA: IEEE Press, 2002.
- [21] L. N. Sharma *et al.*, "Kurtosis-based noise estimation and multiscale energy to denoise ECG signal," *Signal, Image Video Process.*, pp. 1–11, 2011.
- [22] L. Qiao *et al.*, "Ventricular fibrillation and tachycardia classification using a machine learning approach," *IEEE Trans. Biomed. Eng.*, vol. 61, no. 6, pp. 1607–1613, Jun. 2014.
- [23] L. N. Sharma *et al.*, "ECG signal denoising using higher order statistics in wavelet subbands," *Biomed. Signal Process. Control*, vol. 5, no. 3, pp. 214–222, 2010.
- [24] M. Oeff *et al.* (2012). "The PTB diagnostic ECG database," Nat. Metrol. Inst. Germany. [Online]. Available: <http://www.physionet.org/physiobank/database/ptbdb>
- [25] P. E. McSharry *et al.*, "A dynamical model for generating synthetic electrocardiogram signals," *IEEE Trans. Biomed. Eng.*, vol. 50, no. 3, pp. 289–294, Mar. 2003.
- [26] D. S. Fay and K. Gerow, "A biologist's guide to statistical thinking and analysis," in *WormBook: The Online Review of C. Elegans Biology*, 2012.
- [27] C.-J. Huang *et al.*, "Application of wrapper approach and composite classifier to the stock trend prediction," *Expert Syst. Appl.*, vol. 34, no. 4, pp. 2870–2878, 2008.
- [28] A. Kampouraki *et al.*, "Heartbeat time series classification with support vector machines," *IEEE Trans. Inf. Technol. Biomed.*, vol. 13, no. 4, pp. 512–518, Jul. 2009.
- [29] C. Cortes and V. Vapnik, "Support vector machine," *Mach. Learn.*, vol. 20, no. 3, pp. 273–297, 1995.
- [30] J. A. K. Suykens *et al.*, *Least Squares Support Vector Machines*, vol. 4. Singapore: World Scientific, 2002.
- [31] N. Cristianini and J. Shawe-Taylor, *An Introduction to Support Vector Machines and Other Kernel-based Learning Methods*. New York, NY, USA: Cambridge Univ. Press, 2000.
- [32] M. A. Hearst *et al.*, "Support vector machines," *IEEE Trans. Intell. Syst. Appl.*, vol. 13, no. 4, pp. 18–28, Jul./Aug. 1998.
- [33] D. G. Altman and J. M. Bland, "Diagnostic tests 1: Sensitivity and specificity," *Med. Statist. Lab., Imperial Cancer Res. Fund, London*, vol. 308, p. 1552, Jun. 1994.
- [34] R. O. Duda *et al.*, *Pattern Classification*. New York, NY, USA: Wiley, 2012.
- [35] R. K. Tripathy *et al.*, "Artificial intelligence-based classification of breast cancer using cellular images," *RSC Adv.*, vol. 4, no. 18, pp. 9349–9355, 2014.
- [36] W. Tompkins, Ed., *Biomedical Digital Signal Processing*. Englewood Cliffs, NJ, USA: Prentice-Hall, 1993.



L. N. Sharma received the B.Tech. degree in electronics and communication engineering from the North Eastern Regional Institute of Science and Technology, Nirjuli, India, in 1994, and the Master's degree in technology in signal processing and the Ph.D. degree in electronics and electrical engineering from the Indian Institute of Technology Guwahati, India, in 2002 and 2012, respectively.

He joined the Indian Institute of Technology Guwahati in 1996, where he is currently a Technical Officer in the Department of Electronics and Electrical Engineering. He has worked in different research areas like microstrip patch antenna, remote laboratory experiments through Internet, E-governance systems, and digital signal processing. He is involved in Government-funded research and consultancy projects. He has published numbers of papers in international journals and conferences. His current research interests include multivariate and multiscale processing of biomedical signals.



R. K. Tripathy received the B.Tech. degree in electronics and telecommunication engineering from the Biju Patnaik University of Technology, Rourkela, India, in 2009, and the M.Tech. degree in biomedical engineering from the National Institute of Technology Rourkela, India, in 2013. He is currently working toward the Ph.D. degree in the Department of Electronics and Electrical Engineering, Indian Institute of Technology Guwahati, India. His research interests include biomedical signal processing, pattern recognition, and medical image processing.



S. Dandapat (M'99) received the B.E. degree in electrical engineering from Motilal Nehru Regional Engineering College, Allahabad, India, in 1986, the M.Tech. degree in biomedical engineering from the Institute of Technology, Banaras Hindu University, Varanasi, India, in 1991, and the Ph.D. degree in electrical engineering from the Indian Institute of Technology Kanpur, India, in 1997.

He was a Lecturer in electrical engineering at the Indira Gandhi Institute of Technology, Dhenkanal, India, from 1986 to 1989. He was a Reader in the Electrical and Computer Engineering Department, IET, Rohilkhand University, India, from 1996 to 1997. From May 2003 to July 2004, he was a Research Fellow in the Biomedical Engineering Research Center, Nanyang Technological University, Singapore. He joined as an Assistant Professor in the Department of Electronics and Electrical Engineering, Indian Institute of Technology Guwahati, India, in 1997, where he is currently a Professor. His current research interests include digital signal processing, speech processing, biomedical signal processing, and medical image processing.

Dr. Dandapat is a Life Member of the Institution of Engineers, India, and a Life Member of the Biomedical Society of India.